Desalination and Water Treatment
www.deswater.com

doi: 10.5004/dwt.2023.29622

298 (2023) 174–183
June

One-pot solvothermal preparation of MFe_2O_4 (M = Ca, Mg and Ni) ferrite-graphene oxide nanocomposites for adsorption of acridine orange

Huan Wang*, Ruixin Liu, Wei Zhao, Jiale Zhu, Youning Chen, Shan Wang

College of Chemistry and Chemical Engineering, Xianyang Normal University, Xianyang 712000, China, emails: huanwang369@163.com (H. Wang), 1315638281@qq.com (R.X. Liu), xysyzw@126.com (W. Zhao), 2918686653@qq.com (J.L. Zhu), 350219769@qq.com (Y.N. Chen), 331983278@qq.com (S. Wang)

Received 25 December 2022; Accepted 12 May 2023

ABSTRACT

In this paper, MFe_2O_4 (M = Ca, Mg and Ni) ferrite graphene oxide composites (MFe_2O_4-GO) were prepared by a one-pot solvothermal reaction. MFe_2O_4-GO and MFe_2O_4 were characterized by high-resolution transmission electron microscope, X-ray diffraction, thermogravimetric and Fourier-transform infrared spectroscopy. The adsorption performance of MFe_2O_4 and MFe_2O_4-GO were studied using acridine orange as model. The influence factors of adsorption performance such as pH, adsorption time, initial concentration, NaCl concentration and reusability were investigated. The experimental results revealed that the adsorption capacity of MFe_2O_4-GO for acridine orange was significantly higher than that of MFe_2O_4. It can be found that the adsorption capacity of different MFe_2O_4-GO in the following order: $MgFe_2O_4$-GO > $NiFe_2O_4$-GO > $CaFe_2O_4$-GO. The adsorption process of MFe_2O_4-GO for acridine orange conforms to the pseudo-second-order kinetic model and Freundlich isothermal model. MFe_2O_4-GO can be reused five times. The adsorption interaction of acridine orange with MFe_2O_4-GO is mainly electrostatic attraction. MFe_2O_4-GO has practical application value in wastewater treatment as adsorbent.

Keywords: Ferrite; Graphene oxide; Adsorption properties; Acridine orange

1. Introduction

Due to the wide application of synthetic dyes in textile, cosmetics, printing, leather and plastic industries, more than 70,000 tons of dyestuffs are produced around the world every year, and about 100 tons of dyestuffs are into the wastewater [1,2]. At present, dye wastewater has become the great concern of environmental pollutant, and its effective treatment is still a challenge [3]. Acridine orange is a kind of dye with tricyclic aromatic structure, which is widely used in ink, leather, dyeing and other fields. It is a very important pollution source in wastewater. So far, there are many ways to water treatment. For instance, these methods include adsorption [4], oxidation-precipitation method [5], degradation [6], nanomembrane filtration [7], degradation by super/sub-critical water [8] and so on. Among them, adsorption is considered to be a simple, economical and promising method to remove dyes from water [9,10].

To remove dye from wastewater, different adsorbents like activated carbons pellets [11], multiwall carbon nanotubes [12], Ni-Co-S/CTAB nanocomposites [13], hydrolyzed polyacrylamide modified diatomite waste [14], ZnO functionalized high silica zeolitic particles [15] and graphene oxide [16] have been studied. However, the adsorbent is difficult to separate and has low reusability in the adsorption process. Therefore, magnetic adsorbents are employed to remove contaminants from water [17]. Where, ferrite nanomaterials have attracted much attention because of strong adsorption capacity, large specific surface area, simple preparation, low cost and environmental [18,19].

* Corresponding author.

In addition, the magnetic properties of ferrite can solve the technical difficulties of separation and reuse [20,21]. MFe_2O_4 nanoparticles have strong magnetic properties, excellent catalytic properties and mechanical hardness compared with other ferrites [22]. Nonetheless, a drawback of ferrite nanomaterials is their low dispersion in water [23]. At present, ferrites functionalized composites like chitosan [24], SiO_2 [25], polyaniline [26], titania shell [27] and carbon nanotubes [28] have been used to been used to solve the above problems. MFe_2O_4/composites have broad application prospects in nano-biotechnology [29], information storage [30], pollutant removal [31], medical treatment [32], medical diagnosis [33], and drug delivery [34,35]. The hybrid of reduced graphene oxide and ferrite has high photocatalytic activity and adsorption performance because of the addition of reduced graphene [36,37].

In this study, MFe_2O_4 (M = Ca, Mg and Ni) ferrite-graphene oxide nanocomposites were prepared by one-pot solvothermal reaction. The morphology and magnetic properties of MFe_2O_4-GO were investigated. Furthermore, the adsorption capacity of MFe_2O_4-GO (M = Ca, Mg and Ni) for acridine orange in water was also studied and compared. The results showed that MFe_2O_4-GO had high adsorption performance and have broad prospects as adsorbent for removing acridine orange from water.

2. Experimental set-up

2.1. Materials

Scale graphite (99.95%) was purchased from Qingdao Chenyang Graphite Co., Ltd., (China), ferric chloride hexahydrate ($FeCl_3{\cdot}6H_2O$), anhydrous ferric chloride ($FeCl_3$), sodium citrate ($C_6H_5Na_3O_7$) and anhydrous sodium acetate (CH_3COONa) were obtained from Shanghai Sinopharm Chemical Reagent Co., Ltd., nickel sulfate was obtained from Xi'an Chemical Reagent Factory, polyethylene glycol and magnesium nitrate were obtained from Tianjin Comio Chemical Reagent Co., Ltd., anhydrous calcium chloride were purchased from Luoyang Chemical Reagent Factory.

2.2. Preparation of material

2.2.1. Preparation of graphene oxide

Preoxidation of graphite: 20 g of graphite powder were added to 30 mL of concentrated H_2SO_4 containing 10 g $K_2S_2O_8$ and 10 g P_2O_5, which were heated at 80°C for 6 h and cooled to room temperature, then 500 mL distilled water was added carefully and they were placed for 12 h. The solution is filtered and rinsed with distilled water until the filtrate is neutral, and the product is dried.

Preparation of graphene oxide (GO) was on the basis of improved Hummer process [38], 46 mL 98% concentrated sulfuric acid was add into a round bottom three neck bottle, which was cooled with ice water bath, 2.0 g preoxidized graphite was add into strong sulfuric acid slowly, then 6.0 g of potassium permanganate was added gradually and they were kept at 5°C. The reactants was stirred in an ice bath for 1 h, which was stirred at 35°C for 2 h, then 90 mL distilled water was added, the reaction mixture was raised to 98°C for 15 min. After adding 144 mL of warm water, 20 mL of 30 wt.% hydrogen peroxide was poured into. The golden yellow product was centrifuged and filtered, the product was washed to neutral with 5% hydrogen chloride and dried at 60°C. The product was GO.

2.2.2. Preparation of MFe_2O_4-GO

1.68 g ferric chloride hexahydrate, 0.7270 g magnesium nitrate and 0.3 g graphene oxide were added to 150 mL of glycol solution, put them into the ultrasonic cleaner until they were completely dissolved, 10.8 g anhydrous sodium acetate and 3.0 g polyethylene glycol were add to the mixture, which were stirred for 30 min, the obtained viscous colloid was poured into a stainless steel Teflon-lined autoclave and heated at 200°C for 10 h. Then they were washed with anhydrous ethanol for 5 times and dried at 55°C, the product was magnesium ferrite graphite oxide composite material, which was recorded as $MgFe_2O_4$-GO.

The same amount of ferric chloride hexahydrate and graphene oxide were added according to the steps for preparing magnesium ferrite. Other MFe_2O_4-GO (M = Ni and Ca) were synthesized with 0.4390 g nickel sulfate and 0.3441 g anhydrous calcium chloride instead of magnesium nitrate, respectively. MFe_2O_4 (M = Ni and Ca) was also prepared according to the above steps without the addition of graphene oxide.

2.3. Characterization of sample

High-resolution transmission electron microscope of MFe_2O_4 and MFe_2O_4-GO were obtained by a JEM-2100Plus transmission electron microscope (JEOL, Japan). Fourier-transform infrared spectrometry of GO, MFe_2O_4 and MFe_2O_4-GO were determined by a Nicolet iS10 FTIR spectrophotometer (Thermo Fisher Scientific, USA). Scanning electron microscope with energy-dispersive X-ray spectroscopy (SEM-EDS) patterns of samples were obtained by an EVO MA10 scanning electron microscope (ZEISS, Germany). X-ray diffraction spectrum of MFe_2O_4 and MFe_2O_4-GO were carried out by D2 PHASER X-ray diffractometer (Bruker AXS, Germany). Thermogravimetry of GO and MFe_2O_4-GO were performed by TGA heat exchanger (TA instruments, USA), the heating speed was 10°C/min from room temperature to 600°C under the condition of nitrogen. The porosity information of the MFe_2O_4-GO was obtained by ASAP 2460 BET specific surface area and porosity analyzer (Mike, USA). Zeta potential of MFe_2O_4-GO was measured with Zetasizer Nano Series (Malvern, British).

2.4. Adsorption experiments

2.4.1. Adsorption kinetics

Add 0.04 g MFe_2O_4 and 0.04 g MFe_2O_4-GO to two copies of 25.00 mL containing 40 $mg{\cdot}L^{-1}$ acridine orange solution with pH 9.0, respectively. At different adsorption time, the absorbance of the supernatant at 485 nm was determined, and the adsorption capacity was obtained by Eq. (1).

$$q_t = \frac{(c_0 - c_t)v}{m} \tag{1}$$

where q_t (mg·g^{-1}) is the adsorption capacity of adsorbent at time t, c_t (mg·L^{-1}) is the concentration of adsorbate at time t, c_0 (mg·L^{-1}) is the initial concentration of adsorbate, V (L) is the volume of solution, m (g) is the mass of adsorbent.

2.4.2. Adsorption isotherm

0.0100 g of $MgFe_2O_4$-GO were added to 25.00 mL of different concentrations of acridine orange solution (4, 16, 24, 32, 40, 56, and 72 mg·L^{-1}) with pH = 9.0, respectively. The absorbance of supernatant was determined at 485 nm after they were oscillated at 303 K for 12 h. The q_e of $MgFe_2O_4$-GO was obtained by Eq. (2). The q_e of $MgFe_2O_4$-GO at 313 and 323 K were also obtained by the same method.

$$q_e = \frac{(c_0 - c_e)v}{m} \tag{2}$$

where q_e is the adsorption capacity (mg·g^{-1}) of adsorbent at equilibrium, c_e is the concentration (mg·L^{-1}) of adsorbate at equilibrium.

The adsorption isotherm of $NiFe_2O_4$-GO and $CaFe_2O_4$-GO were obtained by the same method.

2.4.3. Effect of pH

Add 0.0100 g MFe_2O_4-GO to 25.00 mL acridine orange solution (40 mg·L^{-1}) with pH at 2.0–11.0, respectively. The other steps followed the determination of adsorption isotherm.

By the same method, the effect of NaCl concentration (0–100 mmol·L^{-1}) on the adsorption performance of MFe_2O_4-GO was studied.

2.4.4. Reusability

0.01 g $MgFe_2O_4$-GO was added to 25.00 mL of 40 mg·L^{-1} acridine orange solution with pH 9.0, which was shaked for 10 h at 303 K and absorbance of supernatant was determined at 485 nm. The adsorption capacity of $MgFe_2O_4$-GO was calculated according to Eq. (2). $MgFe_2O_4$-GO was soaked in 10 mL absolute ethanol for 4 h after magnetic separation, it was rinsed with distilled water for 5 times and dried. The second adsorption experiment was carried out as the above steps. The adsorption–desorption step was repeated for 6 times.

The reusability of $NiFe_2O_4$-GO and $CaFe_2O_4$-GO were determined by the same steps.

3. Results and discussion

3.1. Characterization of samples

3.1.1. Transmission electron microscope

High-resolution transmission electron microscope of $CaFe_2O_4$-GO, $MgFe_2O_4$-GO, and $NiFe_2O_4$-GO were determined to study the morphology and composition of MFe_2O_4-GO (M = Ca, Mg and Ni), as shown in Fig. 1. Fig. 1 indicates that GO of MFe_2O_4-GO was thin layers and covered by a layer of particles, which was attributed to the loading of MFe_2O_4. $CaFe_2O_4$ particles were more dispersed, while $MgFe_2O_4$ and $NiFe_2O_4$ particles were more concentrated and clustered together. The high-resolution transmission electron microscope image of Fig. 1 shows that of MFe_2O_4-GO have lattice spacing of 0.251 and 0.295 nm, which are consistent with (311) and (220) crystal planes of MFe_2O_4-GO. This result was confirmed by the X-ray diffraction pattern of MFe_2O_4-GO.

3.1.2. Fourier infrared spectrum

The infrared spectra of GO, MFe_2O_4 and MFe_2O_4-GO were measured, as shown in Fig. 2. The infrared absorption peaks of GO, MFe_2O_4 and MFe_2O_4-GO at 3,400 cm^{-1} are ascribed to –OH stretching vibrations of H_2O molecules in Fig. 2. The peaks of GO at 1,633; 1,460 and 1,174 cm^{-1} correspond to C=C stretching vibration, C–H bending (scissoring) stretch vibration and C–O–C stretching vibration in GO structure (Fig. 2a). The absorption peaks of MFe_2O_4 and MFe_2O_4-GO at 1,623 cm^{-1} correspond to the bending vibration of –OH caused by the presence of water molecules [39]. The absorption peaks at 1,080 cm^{-1} of $CaFe_2O_4$ and $CaFe_2O_4$-GO correspond to metal–alloy (Fe–Ca), and 580 cm^{-1} are attributed to tetrahedral stretching vibration (Fe–O), indicating the existence of spinel structure $CaFe_2O_4$ [40]. The absorption peaks of $MgFe_2O_4$, $MgFe_2O_4$-GO, $NiFe_2O_4$, $NiFe_2O_4$-GO were also observed at 580 cm^{-1}, which belong to stretching vibration of Fe–O, indicating the existence of $MgFe_2O_4$ [41,42] and $NiFe_2O_4$ [43].

3.1.3. X-ray diffraction spectra

Fig. 3 shows the X-ray diffraction spectra of GO, MFe_2O_4 and MFe_2O_4-GO. The strong diffraction peaks at 11.82° of the X-ray diffraction (XRD) spectra of GO correspond to the crystal planes of (001) in Fig. 3, indicating that the scale graphite has been converted into graphene oxide [44]. The X-ray diffraction spectra of $CaFe_2O_4$ show diffraction peaks at 2θ of 18.43°, 30.33°, 35.71°, 37.42°, 43.33°, 53.73°, 57.21° and 62.93°, which corresponding the crystal faces of (200), (220), (311), (222), (400), (422), (511) and (440) (JCPDS card: 78–4321) [45]. In the XRD spectrum of $CaFe_2O_4$-GO, the diffraction peaks of $CaFe_2O_4$ also appear. The X-ray diffraction spectra of $MgFe_2O_4$ show diffraction peaks at 2θ of 29.86°, 35.33°, 42.90°, 53.34°, 56.82° and 62.49° with the corresponding crystal faces of (220), (311), (400), (422), (511) and (440) (JCPDS card: 17-0406) [46]. In the XRD spectrum of $MgFe_2O_4$-GO, the diffraction peak of $MgFe_2O_4$ also appeared. The XRD spectra of $NiFe_2O_4$ showed diffraction peaks at 2θ of 30.16°, 35.44°, 36.53°, 43.20°, 53.44°, 57.12° and 62.79° with the corresponding (220), (311), (222), (400), (42), (511) and (440) of crystal faces of $NiFe_2O_4$ (JCPDS card: 86-2267) [47]. But in the XRD spectrum of $CaFe_2O_4$-GO, $MgFe_2O_4$-GO and $NiFe_2O_4$-GO, the diffraction peak of GO is not obvious, because GO has the phenomenon of interlayer accumulation with the growth of MFe_2O_4 (M = Ca, Mg and Ni) crystal [48].

3.1.4. Specific surface area and aperture analysis

Brunauer–Emmett–Teller (BET) surface area and porosity of MFe_2O_4-GO were evaluated by N_2 adsorption/

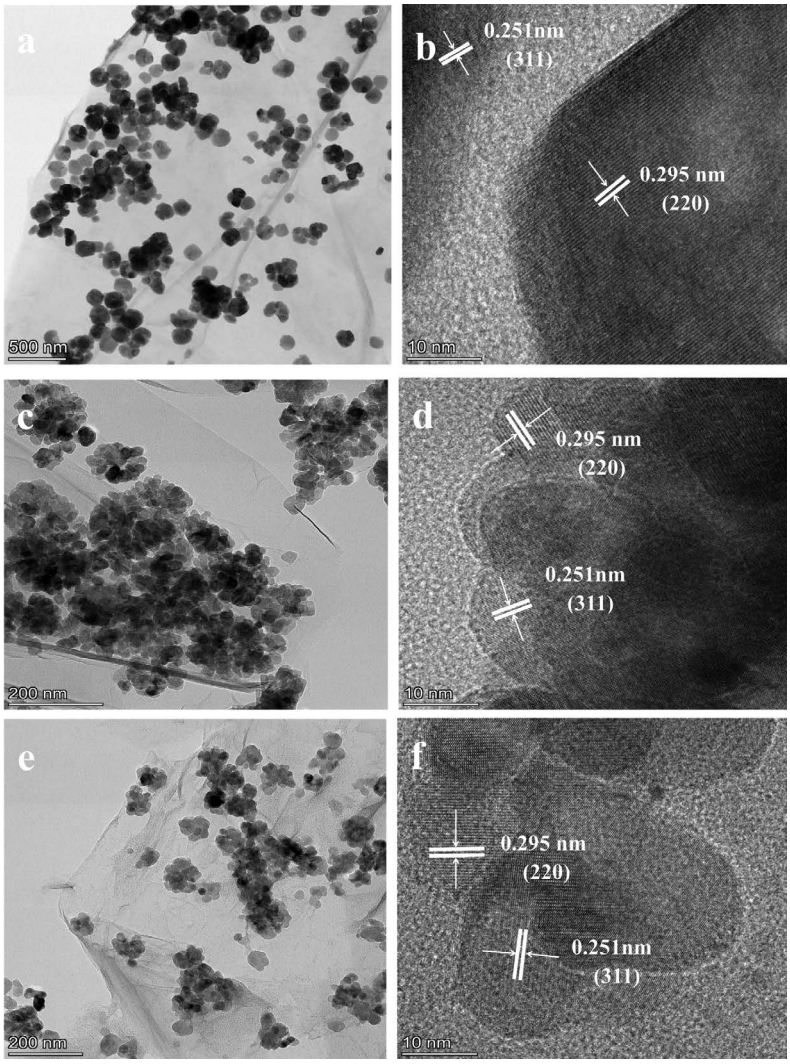

Fig. 1. High-resolution transmission electron microscope of $CaFe_2O_4$-GO (a,b), $MgFe_2O_4$-GO (c,d), and $NiFe_2O_4$-GO (e,f).

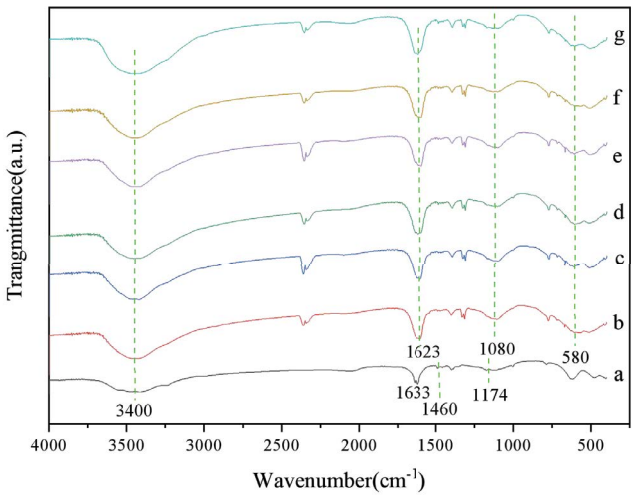

Fig. 2. Fourier-transform infrared spectra of GO (a), $NiFe_2O_4$ (b), $NiFe_2O_4$-GO (c), $MgFe_2O_4$ (d), $MgFe_2O_4$-GO (e), $CaFe_2O_4$ (f) and $CaFe_2O_4$-GO (g).

desorption measurements (Fig. 4). Specifically, the BET surface area of $MgFe_2O_4$-GO (59.5 $m^2 \cdot g^{-1}$) is larger than $CaFe_2O_4$-GO (33.7 $m^2 \cdot g^{-1}$) and $NiFe_2O_4$-GO (17.1 $m^2 \cdot g^{-1}$). Barrett–Joyner–Halenda adsorption average pore diameter of $MgFe_2O_4$-GO (20.1 nm) was narrower than $CaFe_2O_4$-GO (22.7 nm) and $NiFe_2O_4$-GO (25.2 nm), and pore volume of $MgFe_2O_4$-GO (0.3504 $cm^3 \cdot g^{-1}$) was larger than $CaFe_2O_4$-GO (0.2510 $cm^3 \cdot g^{-1}$) and $NiFe_2O_4$-GO (0.1212 $cm^3 \cdot g^{-1}$). So the large specific surface and porosity of $MgFe_2O_4$-GO can offer lots of adsorption sites and promote the diffusion of the adsorbed solution, helping enhance the adsorption performance.

3.1.5. Thermogravimetric analysis

The stability of MFe_2O_4 and MFe_2O_4-GO in nitrogen was determined by thermogravimetry, as shown in Fig. 5. The thermogravimetry curves of MFe_2O_4 are basically unchanged compared with that of MFe_2O_4-GO in Fig. 5. The mass loss of MFe_2O_4-GO is larger with the change of temperature, mainly because of the existence of GO. When the temperature rises from room temperature to 200°C, it is

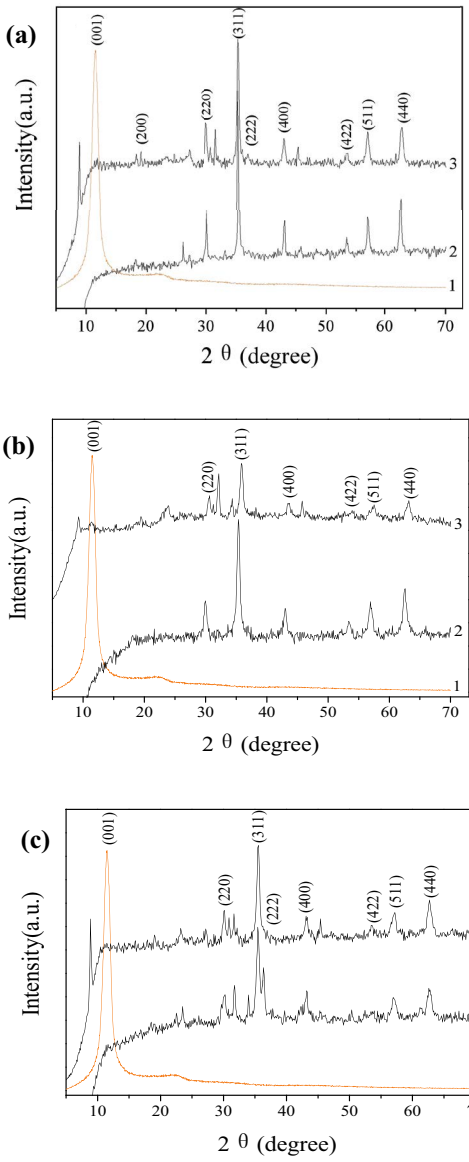

Fig. 3. X-ray diffraction patterns. GO (a1), $CaFe_2O_4$ (a2) and $CaFe_2O_4$-GO (a3); GO (b1), $MgFe_2O_4$ (b2) and $MgFe_2O_4$-GO (b3); GO (c1), $NiFe_2O_4$ (c2) and $NiFe_2O_4$-GO (c3).

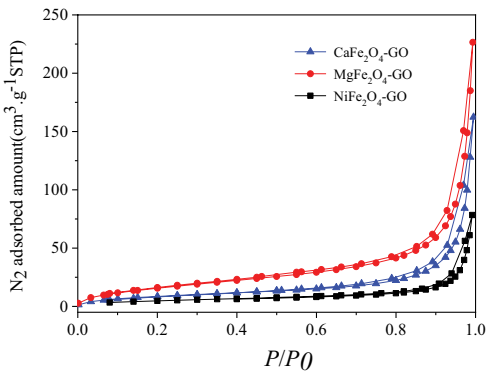

Fig. 4. N_2 adsorption/desorption curve of $CaFe_2O_4$-GO, $MgFe_2O_4$-GO, $NiFe_2O_4$-GO.

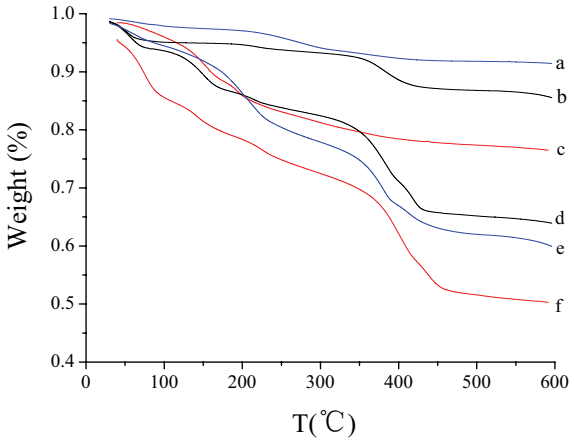

Fig. 5. Thermogravimetry chart $MgFe_2O_4$ (a), $CaFe_2O_4$ (b), $NiFe_2O_4$ (c), $CaFe_2O_4$-GO (d), $MgFe_2O_4$-GO (e) and $NiFe_2O_4$-GO (f).

mainly the loss of absorbed water. When the temperature is 200°C–500°C, it is the loss caused by the decomposition of oxygen-containing groups in MFe_2O_4-GO. When the temperature exceeds 500°C, the weight loss of MFe_2O_4-GO is low. The final weight loss of $CaFe_2O_4$ and $CaFe_2O_4$-GO were 14.44% and 36.08%, the weight loss of $MgFe_2O_4$ and $MgFe_2O_4$-GO were 8.57% and 40.06%, the weight loss of $NiFe_2O_4$ and $NiFe_2O_4$-GO were 23.50% and 46.99%, respectively. The order of weight loss of MFe_2O_4-GO is: $NiFe_2O_4$-GO > $MgFe_2O_4$-GO > $CaFe_2O_4$-GO.

3.1.6. Magnetic analysis

Hysteresis loops of MFe_2O_4-GO (M = Ca, Mg and Ni) are shown in Fig. 6. As can be seen from Fig. 6, MFe_2O_4-GO (M = Ca, Mg and Ni) all have strong magnetic properties, and the order of the magnetic is: $NiFe_2O_4$-GO > $CaFe_2O_4$-GO > $MgFe_2O_4$-GO.

3.2. Adsorption experiments

3.2.1. Comparison of adsorption performance

Adsorption performance of MFe_2O_4-GO (M = Ca, Mg and Ni) for acridine orange were compared with MFe_2O_4 (M = Ca, Mg and Ni), as shown in Fig. 7. Fig. 7 indicates that adsorption capacity of MFe_2O_4-GO (M = Ca, Mg and Ni) for acridine orange were higher than MFe_2O_4 (M = Ca, Mg and Ni), mainly due to the addition of GO. In particular, the adsorption capacity of $MgFe_2O_4$-GO capacity is the largest.

3.2.2. Adsorption kinetics

The adsorption kinetics of MFe_2O_4-GO (M = Ca, Mg and Ni) for acridine orange at pH 9.0 were studied, as shown in Fig. 8. Fig. 8 displays that when the adsorption time reaches 300 min, the adsorption capacity of MFe_2O_4-GO will not increase anymore and the adsorption will reach equilibrium. The adsorption kinetics were fitted by the pseudo-first-order kinetics model and the pseudo-second-

order kinetics model, which can be expressed as Eqs. (3) and (4):

$$\log\left(q_e - q_t\right) = \log q_e - K_1 \frac{t}{2.303} \tag{3}$$

$$\frac{t}{q_t} = \frac{1}{K_2 q_e^2} + \frac{t}{q_e} \tag{4}$$

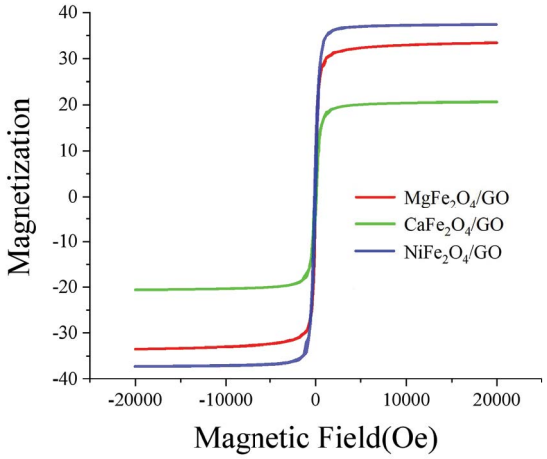

Fig. 6. Magnetic hysteresis loop of $CaFe_2O_4$-GO, $MgFe_2O_4$-GO, $NiFe_2O_4$-GO.

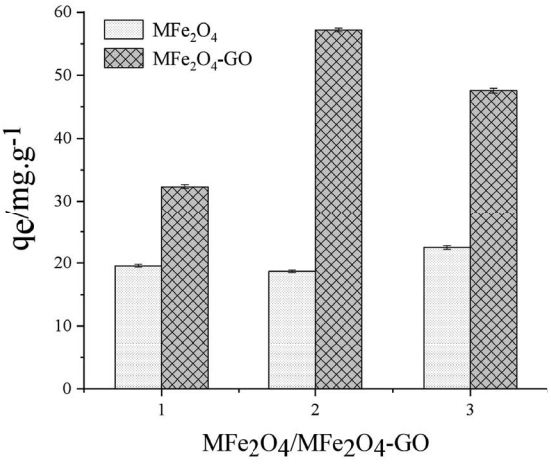

Fig. 7. Comparison of adsorption capacity 1-$CaFe_2O_4$/$CaFe_2O_4$-GO; 2-$MgFe_2O_4$/$MgFe_2O_4$-GO; 3-$NiFe_2O_4$/$NiFe_2O_4$-GO.

where K_1 is the pseudo-first-order adsorption rate constant, K_2 is the pseudo-second-order adsorption rate constant.

Adsorption kinetic parameters of acridine orange on MFe_2O_4-GO (M = Ca, Mg and Ni) at 303 K are displayed in Table 1. The linear correlation coefficient (R^2) of the pseudo-second-order kinetic curve of MFe_2O_4-GO (M = Ca, Mg and Ni) is larger than that of the pseudo-first-order kinetic curve, and q_e of MFe_2O_4-GO (M = Ca, Mg and Ni) calculated from the pseudo-second-order kinetic curve is close to q_{eqex}, so the adsorption of MFe_2O_4-GO (M = Ca, Mg and Ni) for acridine orange is more in line with the pseudo-second-order kinetic model.

3.2.3. Adsorption isotherm

The adsorption isotherm of MFe_2O_4-GO (M = Ca, Mg and Ni) for acridine orange at 293, 303 and 313 K were studied, as shown in Fig. 9.

On the basis of the classical Langmuir and Freundlich adsorption isotherm models, the experimental data of MFe_2O_4-GO (M = Ca, Mg and Ni) for acridine orange were fitted. For ideal monolayer adsorption, the Langmuir equation is as follows:

$$\frac{c_e}{q_e} = \frac{1}{q_m K_L} + \frac{c_e}{q_m} \tag{5}$$

The Freundlich isothermal adsorption model is not limited to single-layer adsorption, which can be used in the case of uneven surfaces. The Freundlich equation is as follows:

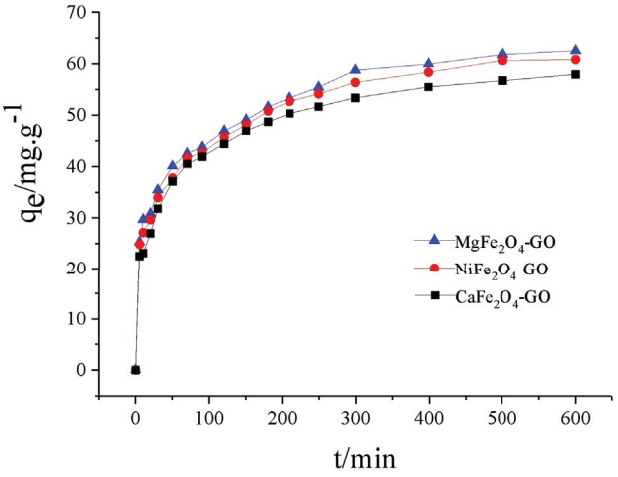

Fig. 8. Adsorption kinetics of MFe_2O_4-GO (M = Ca, Mg and Ni).

Table 1
Adsorption kinetic parameters of MFe_2O_4-GO (M = Ca, Mg and Ni) at 303 K

Adsorbent	q_{eqex} (mg·g^{-1})	Pseudo-first-order kinetics model			Pseudo-second-order kinetics model		
		K_1 (×10^2 min^{-1})	q_e (mg·g^{-1})	R^2	K_2 (×10^3 g·mg^{-1}·min^{-1})	q_e (mg·g^{-1})	R^2
$CaFe_2O_4$-GO	57.94	0.6586	31.73	0.9909	0.6224	58.51	0.9961
$MgFe_2O_4$-GO	62.55	0.6633	34.65	0.9620	0.6432	61.65	0.9913
$NiFe_2O_4$-GO	60.80	0.6702	33.92	0.9689	0.6535	60.10	0.9926

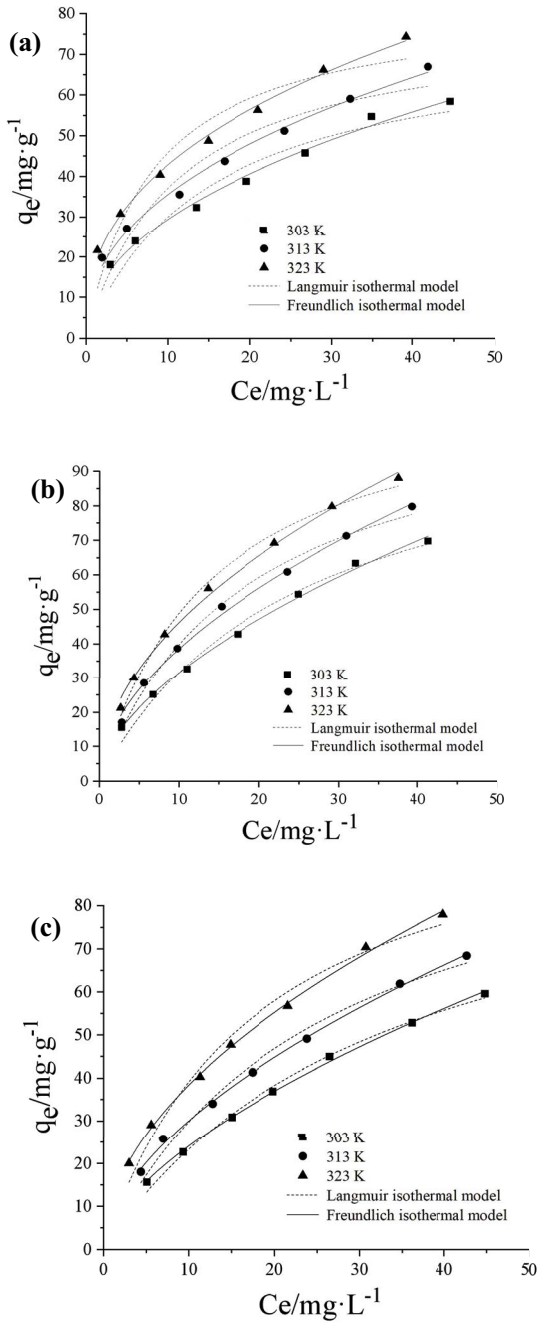

Fig. 9. Adsorption isotherm of $CaFe_2O_4$-GO (a), $MgFe_2O_4$-GO (b) and $NiFe_2O_4$-GO (c).

$$\log q_e = \log K_F + \left[\frac{1}{n}\right]\log c_e \quad (6)$$

In Eqs. (5) and (6), q_{max} (mg·g^{-1}) is the maximum adsorption capacity, K_L (L·mg^{-1}) is the adsorption constants of Langmuir equation, K_F ((mg·g^{-1})(mg·L^{-1})$^{1/n}$) is the adsorption constants of Freundlich equation, n is the temperature related constant. It is generally considered that it is easy to adsorb when $0.1 < 1/n < 0.5$, the adsorption is difficult when $1/n > 2$. Adsorption isothermal parameters of MFe_2O_4-GO (M = Ca, Mg and Ni) are shown in Table 2.

Table 2 shows that coefficient of linear correlation (R^2) of the Freundlich isotherm model is closer to 1, with a higher degree of linear fit, showing that the sample is a monolayer adsorption structure with uniform distribution of active adsorption sites.

3.2.4. Effect of pH

The adsorption capacity of MFe_2O_4-GO (M = Ca, Mg and Ni) for acridine orange was studied with the pH from 2.0 to 11.0, as shown in Fig. 10. The adsorption capacity of MFe_2O_4-GO (M = Ca, Mg and Ni) on acridine orange increased gradually with pH from 2.0 to 9.0, and with pH from 9.0 to 11.0, the adsorption capacity of MFe_2O_4-GO (M = Ca, Mg and Ni) on acridine orange decreased gradually. The optimum pH of MFe_2O_4-GO (M = Ca, Mg and Ni) for acridine orange adsorption was 9.0.

The influence of pH on the adsorption capacity of MFe_2O_4-GO (M = Ca, Mg and Ni) is also connected with the surface charge and structure of acridine orange. acridine orange is a cationic dye with a positive surface charge. At the optimal pH, the surface of MFe_2O_4-GO (M = Ca, Mg and Ni) is negatively charged because of the presence of –COO– and –CO–. The adsorption capacity of MFe_2O_4-GO (M = Ca, Mg and Ni) for acridine orange was the largest because MFe_2O_4-GO had the highest electrostatic attraction with acridine orange. At pH 9.0, the zeta potentials of $MgFe_2O_4$-GO, $CaFe_2O_4$-GO and $NiFe_2O_4$-GO were –32.05, –22.95 and –17.8 mV, respectively. The order of zeta potentials and the specific surface of MFe_2O_4-GO (M = Ca, Mg and Ni) is inconsistent with the order of adsorption capacity MFe_2O_4-GO (M = Ca, Mg and Ni), which is because adsorption plays a leading role in the removal process of acridine orange by MFe_2O_4-GO (M = Ca, Mg and Ni), there is also a photocatalytic effect of MFe_2O_4 (M = Ca, Mg and Ni) [49].

3.2.5. Effect of NaCl

The influence of NaCl on the adsorption performance of MFe_2O_4-GO (M = Ca, Mg and Ni) is shown in Fig. 11. In the range of 0~100 mmol·L^{-1} NaCl concentration, the effect trend of NaCl concentration on MFe_2O_4-GO (M = Ca, Mg and Ni) adsorption capacity is similar. With the increase of NaCl concentration, the adsorption capacity of MFe_2O_4-GO for acridine orange gradually decreases, and finally remained unchanged, which further indicated that the adsorption capacity of MFe_2O_4-GO for acridine orange was mainly affected by electrostatic interaction, and there may be other forces involved.

3.2.6. Recyclability

Fig. 12 shows the change of adsorption capacity of MFe_2O_4-GO (M = Ca, Mg and Ni) for acridine orange after repeated adsorption for six times. It is observed that the initial adsorption capacity of $CaFe_2O_4$-GO, $MgFe_2O_4$-GO and $NiFe_2O_4$-GO for acridine orange were 50.84, 54.91 and 52.84 mg·g^{-1}, respectively. With the increase of

Table 2
Adsorption isothermal parameters of MFe_2O_4-GO at 303, 313 and 323 K

Adsorbent	T (K)	Langmuir equation			Freundlich equation		
		q_m (mg·g^{-1})	K_L (L·mg^{-1})	R^2	K_F (mg·g^{-1})(mg·L^{-1})$^{1/n}$	n	R^2
	303	74.72	0.06717	0.9316	10.12	2.159	0.9897
$CaFe_2O_4$-GO	313	78.89	0.08901	0.9070	13.26	2.335	0.9915
	323	83.27	0.1224	0.9005	17.31	2.539	0.9946
	303	110.1	0.04047	0.9845	8.497	1.751	0.9969
$MgFe_2O_4$-GO	313	113.9	0.05404	0.9911	11.21	1.861	0.9951
	323	117.7	0.07137	0.9916	14.65	2.000	0.9948
	303	103.6	0.02910	0.9933	5.909	1.638	0.9983
$NiFe_2O_4$-GO	313	107.5	0.03840	0.9827	8.085	1.753	0.9982
	323	110.2	0.05514	0.9760	11.61	1.925	0.9980

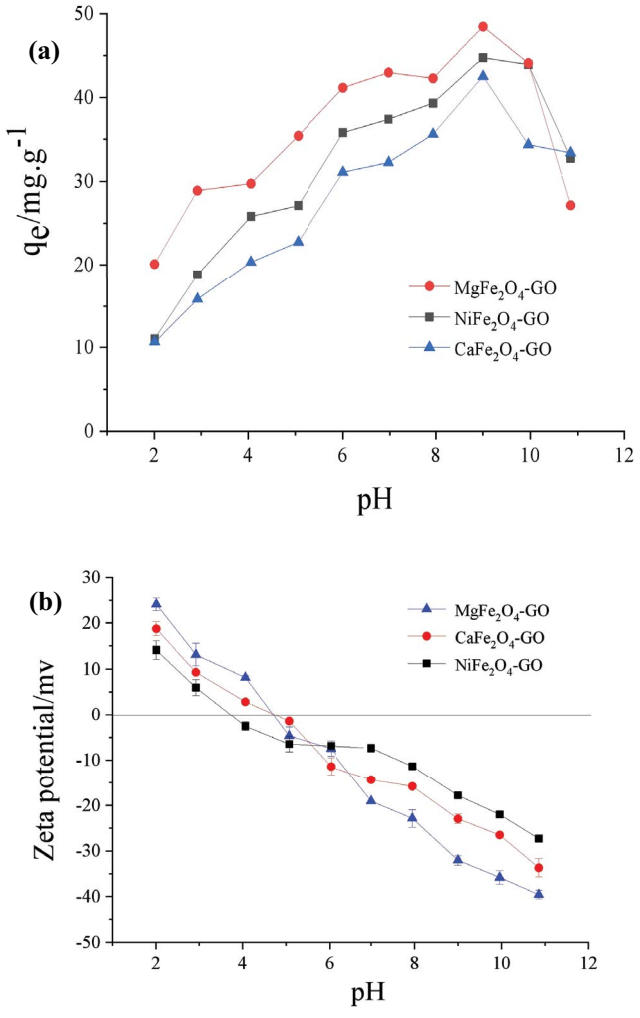

Fig. 10. Effect of pH on (a) adsorption capacity and (b) zeta potential of MFe_2O_4-GO (M = Ca, Mg and Ni).

adsorption times, the adsorption capacity of MFe_2O_4-GO for acridine orange decreased slightly. The adsorption capacity of $CaFe_2O_4$-GO, $MgFe_2O_4$-GO and $NiFe_2O_4$-GO for acridine orange was 21.94, 17.63 and 18.59 mg·g^{-1} at the sixth cycles,

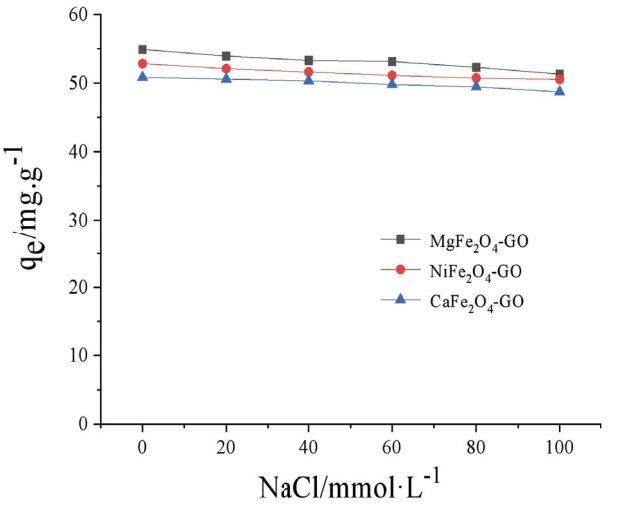

Fig. 11. Effect of NaCl on adsorption capacity of MFe_2O_4-GO (M = Ca, Mg and Ni).

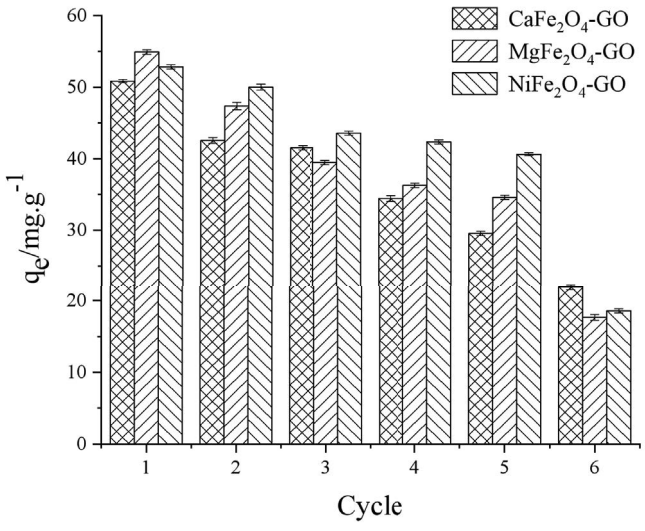

Fig. 12. Reusability of MFe_2O_4-GO (M = Ca, Mg and Ni).

indicating that $CaFe_2O_4$-GO, $MgFe_2O_4$-GO and $NiFe_2O_4$-GO could repeatedly adsorb acridine orange for five times.

4. Conclusion

MFe_2O_4-GO (M = Ca, Mg and Ni) composites were prepared by solvothermal method. The adsorption capacity of MFe_2O_4-GO (M = Ca, Mg and Ni) for acridine orange were investigated. The experimental results showed that the adsorption capacity of MFe_2O_4-GO (M = Ca, Mg and Ni) for acridine orange was significantly higher than that of MFe_2O_4. The adsorption of MFe_2O_4-GO for acridine orange conforms to pseudo-second-order kinetics model and Freundlich isothermal model. The adsorption of MFe_2O_4-GO for acridine orange was mainly by electrostatic attraction, and MFe_2O_4-GO could be reused for five times.

Acknowledgements

This work was supported by Shaanxi Province Science and Technology Plan Project of China (No.2021JQ-815), Xianyang Science and Technology Research Project of China (No. 2021ZDYF-SF-0025, L2022-XCZX-002), Xianyang City Qinchuangyuan science and technology innovation special project (No. L2022-QCYZX-GY-006), Science and Technology Research Project of Xianyang Normal University (No. XSYK20017), Blue Talent Project of Xianyang Normal University (No. XSYQL202002), National College Students Innovation and Entrepreneurship Project of China (No.202110722010) and College Students' Innovation and Entrepreneurship Team Project of Xianyang Normal University (No. XSYC202134).

References

[1] S.K. Sonar, P.S. Niphadkar, S. Mayadevi, P.N. Joshi, Preparation and characterization of porous fly ash/$NiFe_2O_4$ composite: promising adsorbent for the removal of Congo red dye from aqueous solution, Mater. Chem. Phys., 148 (2014) 371–379.
[2] M. Azami, M. Bahram, S. Nouri, Central composite design for the optimization of removal of the azo dye, Methyl Red, from wastewater using Fenton reaction, Curr. Chem. Lett., 2 (2013) 57–68.
[3] G. Gebreslassiea, P. Bharalia, U. Chandra, A. Sergawie, P.K. Boruahd, M.R. Dasd, E. Alemayehu, Novel g-C_3N_4/graphene/$NiFe_2O_4$ nanocomposites as magnetically separable visible light driven photocatalysts, J. Photochem. Photobiol., A, 382 (2019) 111960–111970.
[4] M. Daoud, O. Benturki, P. Girods, A. Donnot, S. Fontana, Adsorption ability of activated carbons from *Phoenix dactylifera rachis* and *Ziziphus jujube* stones for the removal of commercial dye and the treatment of dyestuff wastewater, Microchem. J., 148(2019) 493–502.
[5] C. Anushree, J. Philip, Efficient removal of methylene blue dye using cellulose capped Fe_3O_4 nanofluids prepared using oxidation-precipitation method, Colloids Surf., A, 567 (2019) 193–204.
[6] A. Akbari, Z. Sabouri, H.A. Hosseini, A. Hashemzadeh, M. Khatami, M. Darroudi, Effect of nickel oxide nanoparticles as a photocatalyst in dyes degradation and evaluation of effective parameters in their removal from aqueous environments, Inorg. Chem. Commun., 115 (2020) 107867, doi: 10.1016/j.inoche.2020.107867.
[7] N. Rabiee, Y. Fatahi, M. Asadnia, H. Daneshgar, M. Kiani, A.M. Ghadiri, M. Atarod, A.H. Mashhadzadeh, O. Akhavan, M. Bagherzadeh, E.C. Lima, M.R. Saeb, Green porous benzamide-like nanomembranes for hazardous cations detection, separation, and concentration adjustment, J. Hazard. Mater., 423 (2022) 127130, doi: 10.1016/j.jhazmat.2021.127130.
[8] M. Jouyandeh, O. Tavakoli, R. Sarkhanpour, S.M. Sajadi, P. Zarrintaj, N. Rabiee, O. Akhavan, E.C. Lima, M.R. Saeb, Green products from herbal medicine wastes by subcritical water treatment, J. Hazard. Mater., 424 (2022) 127294, doi: 10.1016/j.jhazmat.2021.127294.
[9] Y. Chao, W. Zhu, X. Wu, F. Hou, S. Xun, P. Wu, H. Ji, H. Xu, H. Li, Application of graphene-like layered molybdenum disulfide and its excellent adsorption behavior for doxycycline antibiotic, Chem. Eng. J., 243 (2014) 60–67, doi: 10.1016/j.cej.2013.12.048.
[10] F. Liu, W. Zhang, W. Chen, J. Wang, Q. Yang, W. Zhu, J. Wang, One-pot synthesis of $NiFe_2O_4$ integrated with EDTA-derived carbon dots for enhanced removal of tetracycline, Chem. Eng. J., 310 (2017) 187–196.
[11] S.H. Tang, M.A.A. Zaini, Development of activated carbon pellets using a facile low-cost binder for effective malachite green dye removal, J. Cleaner Prod., 253 (2020) 119970, doi: 10.1016/j.jclepro.2020.119970.
[12] O.A. Shabaan, H.S. Jahin, G.G. Mohamed, Removal of anionic and cationic dyes from wastewater by adsorption using multiwall carbon nanotubes, Arabian J. Chem., 13 (2020) 4797–4810.
[13] A. Chowdhury, S. Kumari, A.A. Khan, S. Hussain. Selective removal of anionic dyes with exceptionally high adsorption capacity and removal of dichromate ($Cr_2O_7^{2-}$) anion using Ni-Co-S/CTAB nanocomposites and its adsorption mechanism, J. Hazard. Mater., 385 (2020) 121602, doi: 10.1016/j.jhazmat.2019.121602.
[14] T. Ma, Y. Wu, N. Liu, Y. Wu, Hydrolyzed polyacrylamide modified diatomite waste as a novel adsorbent for organic dye removal: adsorption performance and mechanism studies, Polyhedron, 175 (2020) 114227, doi: 10.1016/j.poly.2019.114227.
[15] S. Madan, R. Shaw, S. Tiwari, S.K. Tiwari, Adsorption dynamics of Congo red dye removal using ZnO functionalized high silica zeolitic particles, Appl. Surf. Sci., 487 (2019) 907–917.
[16] A. Bhattacharyya, D. Mondal, I. Roy, G. Sarkar, N.R. Saha, D. Rana, T.K. Ghosh, D. Mandal, M. Chakraborty, D. Chattopadhyay, Studies of the kinetics and mechanism of the removal process of proflavine dye through adsorption by graphene oxide, J. Mol. Liq., 230 (2017) 696–704.
[17] C.L. Warner, W. Chouyyok, K.E. Mackie, D. Neiner, L.V. Saraf, T.C. Droubay, M.G. Warner, R.S. Addleman, Manganese doping of magnetic iron oxide nanoparticles: tailoring surface reactivity for a regenerable heavy metal sorbent, Langmuir, 28 (2012) 3931–3937.
[18] H. Zeng, P.M. Rice, S.X. Wang, S. Sun, Shape-controlled synthesis and shape-induced texture of $MnFe_2O_4$ nanoparticles, J. Am. Chem. Soc., 126 (2004) 11458–11459.
[19] X. Bao, Z. Qiang, W. Ling, J.-H. Chang, Sonohydrothermal synthesis of MFe_2O_4 magnetic nanoparticles for adsorptive removal of tetracyclines from water, Sep. Purif. Technol., 117 (2013) 104–110.
[20] N.R. Su, P. Lv, M. Li, X. Zhang, M. Li, J. Niu, Fabrication of $MgFe_2O_4$-ZnO heterojunction photocatalysts for application of organic pollutants, Mater. Lett., 122 (2014) 201–204.
[21] W. Fan, M. Li, H. Bai, D. Xu, C. Chen, C. Li, Y. Ge, W. Shi, Fabrication of $MgFe_2O_4/MoS_2$ heterostructure nanowires for photoelectrochemical catalysis, Langmuir, 32 (2016) 1629–1636.
[22] Y. Xia, Z. He, J. Su, B. Tang, K. Hu, Y. Lu, S. Sun, X. Li, Fabrication of magnetically separable $NiFe_2O_4$BiOI nanocomposites with enhanced photocatalytic performance under visible-light irradiation, RSC Adv., 8 (2018) 4284–4294.
[23] S. Ma, S. Zhan, Y. Jia, Q. Zhou, Highly efficient antibacterial and Pb(II) removal effects of Ag-$CoFe_2O_4$-GO nanocomposite, ACS Appl. Mater. Interfaces, 7 (2015) 10576–10586.
[24] A.Z. Moghaddam, E. Ghiamati, A. Pourashuri, A. Allahresani, Modified nickel ferrite nanocomposite/functionalized chitosan as a novel adsorbent for the removal of acidic dyes, Int. J. Biol. Macromol., 120 (2018) 1714–1725.
[25] M. Amiri, M. Salavati-Niasari, A. Akbari, T. Gholami, Removal of malachite green (a toxic dye) from water by cobalt ferrite

silica magnetic nanocomposite: herbal and green sol–gel autocombustion synthesis, Int. J. Hydrogen Energy, 42 (2017) 24846–24860.
[26] P. Kharazi, R. Rahimi, M. Rabbani, Copper ferrite-polyaniline nanocomposite: structural, thermal, magnetic and dye adsorption properties, Solid State Sci., 93 (2019) 95–100.
[27] T. Tatarchuk, I. Mironyuk, V. Kotsyubynsky, A. Shyichuk, M. Myslin, V. Boychuk, Structure, morphology and adsorption properties of titania shell immobilized onto cobalt ferrite nanoparticle core, J. Mol. Liq., 297 (2020) 111757, doi: 10.1016/j.molliq.2019.111757.
[28] D. Wu, G. Lu, J. Yao, C. Zhou, F. Liu, J. Liu, Adsorption and catalytic electro-peroxone degradation of fluconazole by magnetic copper ferrite/carbon nanotubes, Chem. Eng. J., 370 (2019) 409–419.
[29] M.J. Hajipour, O. Akhavan, A. Meidanchi, S. Laurent, M. Mahmoudi, Hyperthermia-induced protein corona improves the therapeutic effects of zinc ferrite spinel-graphene sheets against cancer, RSC Adv., 4 (2014) 62557–62565.
[30] R. Sharma, P. Thakur, P. Sharma, V. Sharma, Ferrimagnetic Ni^{2+} doped Mg-Zn spinel ferrite nanoparticles for high density information storage, J. Alloys Compd., 704 (2017) 7–17.
[31] K.K. Kefeni, B.B. Mamba, T.A.M. Msagati, Application of spinel ferrite nanoparticles in water and wastewater treatment: a review, Sep. Purif. Technol., 188 (2017) 399–422.
[32] A. Meidanchi, O. Akhavan, S. Khoei, A. Shokri, Z. Hajikarimi, N. Khansari, $ZnFe_2O_4$ nanoparticles as radiosensitizers in radiotherapy of human prostate cancer cells, Mater. Sci. Eng., C, 46 (2015) 394–399.
[33] H. Zhang, L. Li, X. Liu, J. Jiao, C.-T. Ng, J. Yi, Y. Luo, B.-H. Bay, L. Zhao, M. Peng, N. Gu, H. Fan, Ultrasmall ferrite nanoparticles synthesized via dynamic simultaneous thermal decomposition for high-performance and multi-functional T_1 magnetic resonance imaging contrast agent, ACS Nano, 11 (2017) 3614–3631.
[34] O. Akhavan, A. Meidanchi, E. Ghaderi, S. Khoei, Zinc ferrite spinel-graphene in magneto-photothermal therapy of cancer, J. Mater. Chem. B, 2 (2014) 3306–3314.
[35] H. Deng, X. Li, Q. Peng, X. Wang, J. Chen, Y. Li, Monodisperse magnetic single-crystal ferrite microspheres, Angew. Chem. Int. Ed. Engl., 44 (2005) 2782–2785.
[36] A. Shabbir, S. Ajmal, M. Shahid, I. Shakir, P.O. Agboola, M.F. Warsi. Zirconium substituted spinel nano-ferrite $Mg_{0.2}Co_{0.8}Fe_2O_4$ particles and their hybrids with reduced graphene oxide for photocatalytic and other potential applications, Ceram. Int., 45 (2019) 16121–16129.
[37] L.P. Lingamdinne, Y.-L. Choi, I.-S. Kim, J.-K. Yang, J.R. Koduru, Y.-Y. Chang, Preparation and characterization of porous reduced graphene oxide based inverse spinel nickel ferrite nanocomposite for adsorption removal of radionuclides, J. Hazard. Mater., 326 (2017) 145–156.
[38] L. Sun, H. Yu, B. Fugetsu, Graphene oxide adsorption enhanced by in situ reduction with sodium hydrosulfite to remove acridine orange from aqueous solution, J. Hazard. Mater., 203–204 (2012) 101–110.
[39] Z. Jia, Q. Wang, D. Ren, R. Zhu, Fabrication of one-dimensional mesoporous a-Fe_2O_3 nanostructure via self-sacrificial template and its enhanced Cr(VI) adsorption capacity, Appl. Surf. Sci., 264 (2013) 255–260.
[40] L. Khanna, N.K. Verma, PEG/$CaFe_2O_4$ nanocomposite: Structural, morphological, magnetic and thermal analyses, Physica B, 427 (2013) 68–75.
[41] R.H. Vignesh, K.V. Sankar, S. Amaresh, Y.S. Lee, R.K. Selvan, Synthesis and characterization of $MnFe_2O_4$ nanoparticles for impedometric ammonia gas sensor, Sens. Actuators, A, 220 (2015) 50–58.
[42] Y. Zhou, B. Xiao, S.-Q. Liu, Z. Meng, Z.-G. Chen, C.-Y. Zou, C.-B. Liu, F. Chen, X. Zhou, Photo-Fenton degradation of ammonia via a manganese–iron double active component catalyst of graphene–manganese ferrite under visible light, Chem. Eng. J., 283 (2016) 266–275.
[43] P.A. Udhaya, M. Meena, Albumen assisted green synthesis of $NiFe_2O_4$ nanoparticles and their physico-chemical properties, Mater. Today: Proc., 9 (2019) 528–534.
[44] S. Chella, P. Kollu, E.V.P.R. Komarala, S. Doshi, M. Saranya, S. Felix, R. Ramachandran, P. Saravanan, V.L. Koneru, V. Venugopal, S.K. Jeong, A.N. Grace, Solvothermal synthesis of $MnFe_2O_4$-graphene composite—investigation of its adsorption and antimicrobial properties, Appl. Surf. Sci., 327 (2015) 27–36.
[45] G. Wang, D. Zhao, Y. Ma, Z. Zhang, H. Che, J. Mu, X. Zhang, Y. Tong, X. Dong, Synthesis of calcium ferrite nanocrystal clusters for magnetorheological fluid with enhanced sedimentation stability, Powder Technol., 322 (2017) 47–53.
[46] Z. Jiang, K. Chen, Y. Zhang, Y. Wang, F. Wang, G. Zhang, D.D. Dionysiou, Magnetically recoverable $MgFe_2O_4$/conjugated polyvinyl chloride derivative nanocomposite with higher visible-light photocatalytic activity for treating Cr(VI)-polluted water, Sep. Purif. Technol., 236 (2020) 116272, doi: 10.1016/j.seppur.2019.116272.
[47] S. Zhang, W. Jiang, Y. Li, X. Yang, P. Sun, F. Liu, X. Yan, Y. Gao, X. Liang, J. Ma, G. Lu, Highly-sensitivity acetone sensors based on spinel-type oxide ($NiFe_2O_4$) through optimization of porous structure, Sens. Actuators, B, 291 (2019) 266–274.
[48] P. Xiong, C. Hu, Y. Fan, W. Zhang, J. Zhu, X. Wang, Ternary manganese ferrite/graphene/polyaniline nanostructure with enhanced electrochemical capacitance performance, J. Power Sources, 266 (2014) 384–392.
[49] P. Veisi, M.S.S. Dorraji, M.H. Rasoulifard, S. Ghaffari, A.K. Choobar, Synergistic photocatalytic-adsorption removal effect of $NiFe_2O_4$-Zn-Al mixed metal oxide composite under visible-light irradiation, J. Photochem. Photobiol., A, 414 (2021) 113268–113283.